


SCIENTIFIC REPORTS

OPEN

The crucial role of density functional nonlocality and on-axis CH_3NH_3 rotation induced I_2 formation in hybrid organic-inorganic $\text{CH}_3\text{NH}_3\text{PbI}_3$ cubic perovskite

Rakchat Klinkla^{1,2}, Vichawan Sakulsupich^{1,2}, Teerachote Pakornchote^{1,2}, Udomsilp Pinsook^{1,2} & Thiti Bovornratanaraks^{1,2} 

Effects of electronic nonlocality in density functional theory study of structural and energetic properties of a pseudocubic $\text{CH}_3\text{NH}_3\text{PbI}_3$ are investigated by considering coherent rotation around C–N axis of a CH_3NH_3 cation. A number of truly non-local and semi-local exchange correlation density functionals are examined by comparing calculated structural parameters with experimental results. The vdW-DF-cx which takes into account the non-local van der Waals correlation and consistent exchange shows the best overall performance for density functional theory study of this system. Remarkable distinctions between results from vdW-DF-cx and those from PBEsol exchange correlation functionals are observed and indicate the need of including the non-local interaction in the study of this system, especially its dynamical properties. The obtained rotational barriers are 18.56 meV/formula and 27.71 meV/formula which correspond to rotational frequencies of 3.71 THz and 2.60 THz for vdW-DF-cx and PBEsol calculations, respectively. Interestingly, the maximally localised Wannier function analysis shows the hydrogen bonding assisted covalent character of two iodide anions at a moderate rotational angle which can lead to I_2 formation and then material degradation.

In the last decade, there has been a booming interest in hybrid organic inorganic perovskites (HOIPs) originates from their potential applications in optoelectronic, thermoelectric, and photovoltaic technologies, owing to their favourable electronic, excitonic and optical properties^{1–4}. In only ten years' time, reported power conversion efficiencies of perovskite solar cells have been raised up from the first record of 2.2% in 2009, to 22.1% in 2016^{2,5,6}. Intensive researches have rendered perovskite solar cells into devices that are both easy to fabricate and have high cell power conversion efficiency, on par with those of silicon solar cells⁷. But commercial perovskite photovoltaic devices are still several years down the road, due to its stability issues^{8–11}.

HOIPs are in a class of material that has a perovskite crystal structure with an ABX_3 chemical composition, where A, B, and X represent an organic monovalent cation, an inorganic cation and a halogen, respectively. Methylammonium lead iodide (MAPbI_3) perovskite, which, as the name suggested, has methylammonium (MA) as the cation, is regarded as the archetype of HOIPs since it exhibits rich fundamental photovoltaic properties, and has recently been intensively studied and developed for solar cell devices. MAPbI_3 exists in three phases, namely orthorhombic (Pnma) at $0\text{ K} < T < 165\text{ K}$, tetragonal (I4/mcm) at $165\text{ K} < T < 327\text{ K}$, and cubic ($\text{Pm}\bar{3}\text{m}$) at $T > 327\text{ K}$ with ordered antiferroelectric MA cation arrangement for the first, and disordered arrangements for the latter two^{12–15}. Orientation dynamics of the organic cations are associate with physical properties of MAPbI_3 . One is the ferroelectric effect which is related to an anomalous hysteresis in the HOIP solar cells¹⁶. Long migration length of electrons and holes¹⁷, structural evolution and stability also result from the said dynamics^{14,15,18–24}.

¹Extreme Conditions Physics Research Laboratory, Physics of Energy Materials Research Unit, Department of Physics, Faculty of Science, Chulalongkorn University, Bangkok, 10330, Thailand. ²Thailand Center of Excellence in Physics, Commission on Higher Education, 328 SiAyutthaya Road, Bangkok, 10400, Thailand. Correspondence and requests for materials should be addressed to T.B. (email: Thiti.b@chula.ac.th)

Structural parameters (Å)	\bar{a}	$\overline{\text{PbI}}$	MAE(1)	CN	$\overline{\text{CH}}$	$\overline{\text{NH}}$	MAE(2)
PBE	6.471(0.2)	3.205(0.05)	0.1000	1.492(0.1)	1.094(0.1)	1.040(0.05)	0.097
PBEsol	6.299(0.02)	3.146(0.01)	0.0156	1.484(0.1)	1.100(0.1)	1.047(0.05)	0.098
rVV10	6.373(0.06)	3.183(0.02)	0.0404	1.503(0.2)	1.093(0.1)	1.040(0.05)	0.100
vdW-DF	6.554(0.2)	3.237(0.08)	0.1576	1.513(0.2)	1.090(0.1)	1.036(0.04)	0.101
vdW-DF2	6.562(0.3)	3.258(0.1)	0.1721	1.524(0.2)	1.087(0.1)	1.036(0.04)	0.104
vdW-DF2-b86r	6.357(0.04)	3.173(0.01)	0.0268	1.496(0.2)	1.097(0.1)	1.043(0.05)	0.100
vdW-DF-cx	6.320(0.003)	3.149(0.01)	0.0061	1.493(0.2)	1.098(0.1)	1.044(0.05)	0.100
vdW-DF-ob86	6.329(0.01)	3.153(0.006)	0.0083	1.497(0.2)	1.097(0.1)	1.043(0.05)	0.100
Exp.	6.317(0.0)	3.159(0.0)	—	1.348(0.0)	0.994(0.0)	0.994(0.0)	—

Table 1. Calculated average structural parameters using semi-local and non-local vdW-DFs compared with experimental results¹⁵. The numbers in parentheses stand for deviation of calculated values from experimental ones. MAE(1) and MAE(2) are mean absolute error of subgroups of parameters $\{\bar{a}, \overline{\text{PbI}}\}$ and $\{\text{CN}, \overline{\text{CH}}, \overline{\text{NH}}\}$, respectively.

Recent experimental results suggest that there exist two kinds of dynamics associated with a MA cation in MAPbI₃²³. The first type is the reorientation of the C–N axis with estimated 3–14 ps time scale^{16,17,19,23}. The second type is the much faster methyl and/or ammonium groups rotation about C–N axis with sub-picosecond time scale²⁵ that has recently been estimated at ~30 times faster²⁶. Such fast-rotation cannot be precisely probed by experiments²³. Moreover, the interplay between octahedron tilting and the MA dynamics still needs a clearer understanding, as it has recently been dubbed as the chicken-and-egg paradox by Li and Rinke²⁷.

Since the emergence of HOIPs as photovoltaic materials in 2009², density functional theory (DFT) based calculations have been adopted to study their properties and underlying physics. Most of the studies are based on the standard semi-local generalised gradient approximation which cannot retain the non-local nature of electron correlation. However, many suggest the importance of including the non-local van der Waals (vdW) interaction in the calculations to recover such many-body effect^{24,27–31}. Nevertheless, there are a number of methods for including the vdW-interaction implemented in the DFT based software packages. Each of them yields different levels of accuracy, especially, for molecular, sparse and hydrogen-bond materials. The detailed discussions on the methodology and accuracy of the vdW density functionals (vdW-DFs) can be found elsewhere^{32–34}.

In this work, we examine the application of various vdW-DFs and discuss in detail the equilibrium structural configurations corresponding to the on-axis MA rotation obtained by structural relaxations. As a result, vdW-DF-cx non-local exchange correlation (xc) functional shows the best overall performance for this system with some remarkable differences in the atomic configurations comparing with those of PBEsol semi-local xc-functional. By adding the non-local effect, lowering and broadening of the rotational energy barrier are observed. Furthermore, maximally localised Wannier function (MLWF) analysis illustrates the formation of hydrogen bond assisted I–I covalent bonding at a specific MA rotational angle which could lead to the formation of neutral I₂ defect and so the material degradation.

Results and Discussion

Structural parameters. First, we examine the xc-functionals by calculating structural parameters of the pseudocubic MAPbI₃ unit cell. Since the assigned Pm $\bar{3}$ m symmetry of MAPbI₃ was derived from the average structure of the material at high temperature. Therefore, the average values of such calculated parameters, i.e. average lattice constant (\bar{a}), average Pb–I bond length over three inequivalent I-atoms ($\overline{\text{PbI}}$), average C–H bond length ($\overline{\text{CH}}$), average N–H bond length ($\overline{\text{NH}}$), and C–N bond length (CN) obtained by performing full structural relaxation, there is no any constraint, where the C–N axis is at the lowest enthalpy arrangement¹⁴, are used for the comparison with Weller *et al.*'s accurate powder neutron diffraction experimental results¹⁵.

The structural parameters are grouped into two subgroups according to magnitudes of their absolute errors, i.e. \bar{a} and $\overline{\text{PbI}}$ as one subgroup and CN, $\overline{\text{CH}}$ and $\overline{\text{NH}}$ as the other. The mean absolute error (MAE) of each subgroup is given in Table 1. The parameters \bar{a} and $\overline{\text{PbI}}$ are in excellent agreement with experimental results (MAE(1) < 1%) for most of xc-functionals except for vdW-DF, vdW-DF2, and PBE. Notably, the vdW-DF-cx shows the best performance in predicting the lattice constant and the Pb–I distance, see MAE(1) in Table 1. This is in good agreement with the vdW-DF testing performed by Berland and Hyldgaard. They examined the accuracy of a number of vdW-DFs in predicting the binding energy and equilibrium separation in H-bond and dispersive-force dominated systems and found that vdW-DF-cx shows the best overall performance³². However, MAE(2) in Table 1 shows that errors in CN, $\overline{\text{CH}}$, and $\overline{\text{NH}}$ are in approximately the same order for all xc-functionals, with an error of ~10% for CN and $\overline{\text{CH}}$, and ~5% for $\overline{\text{NH}}$. The disordered C–N axis orientation and the fast on-axis rotation of H-atoms could probably be responsible for the errors in structural parameters. The divergence from the experimental data might originate from the indistinguishability of the atomic position reported by the experiment. Since the position of C, N, H_C and H_N atoms cannot be experimentally captured due to the MA dynamics, their positions are approximately assigned to Wyckoff sites 4MM(100) and 1 of the Pm $\bar{3}$ m space group¹⁵. From the simulation viewpoint, by using only one pseudocubic primitive unit cell, the disordered nature of the organic cations is neglected, giving rise to the divergence from averaged value of the experimental data. Moreover, the effects of temperature which drive atoms from their zero-Kelvin equilibrium configurations are also not included. Although the simulations give large MAE(2), the lattice constant and the Pb–I bond length are in good agreement

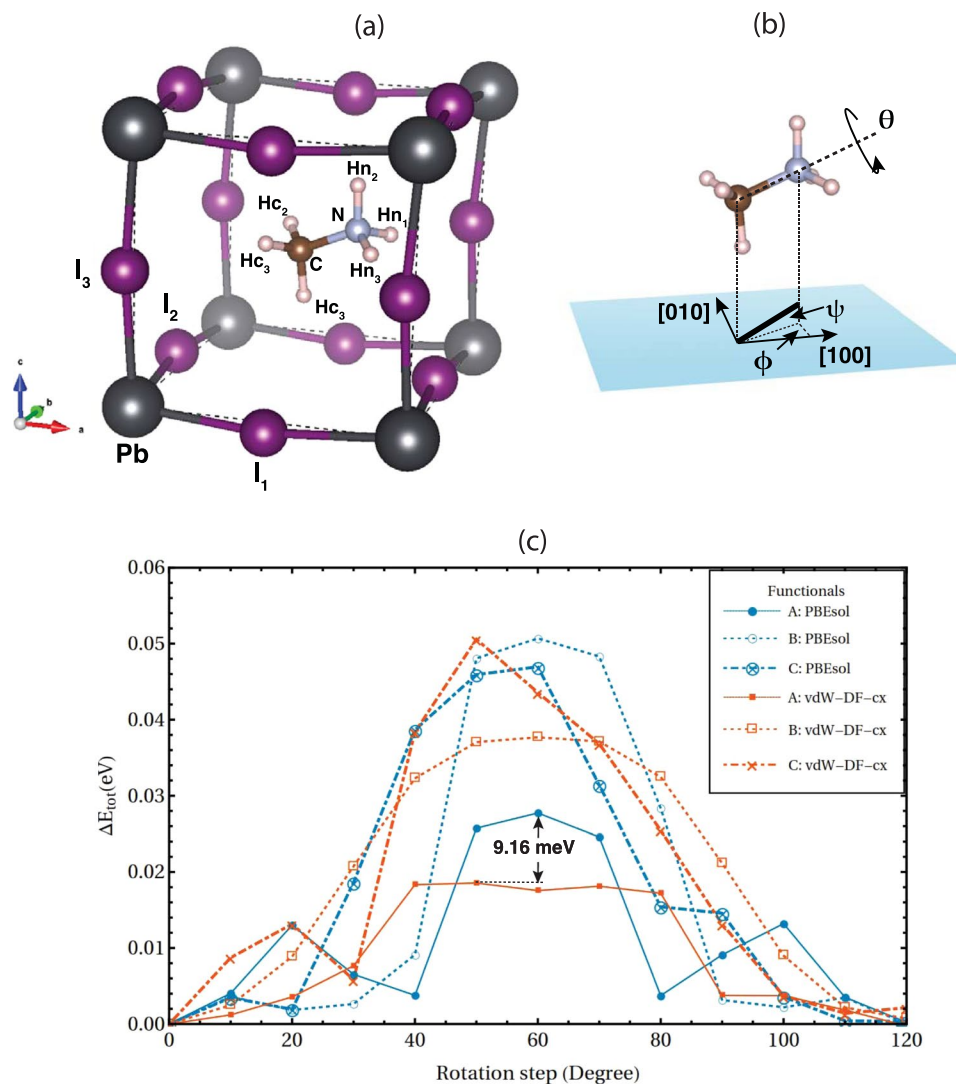


Figure 1. (a) Atomistic model of a unit cell. (b) Parameters that describe MA orientation (φ , ψ), and rotation (θ). (c) Rotational barriers obtained by performing structural relaxation with: (A) no any constraint, (B) fixed cell parameters at initial structure, and (C) fixed cell parameters and I-atomic position at initial structure.

with those of the experimental results, thanks to their low dynamics. The latter validates the use of computational model for investigating the local structural and energetic responses to the rotation of H atoms about the C-N axis.

Energy barriers, Equilibrium atomic configurations, and H-bonds. The rotational energy barriers are obtained by performing structural relaxation without any constraint after coherent H-atoms rotation (solid lines in Fig. 1(c)). The rotation of MA is discretised to 12 rotational steps with 10° step size owing to its C_{3v} symmetry, see Fig. 1 for atomistic structural model. Hereafter, only the results from vdW-DF-cx and PBEsol xc-functionals are shown as they are the representatives of non-local and semi-local xc-functionals respectively, results from all xc-functionals are provided in supplementary information. According to Fig. 1(c), the rotational potential energy, $\Delta E(\theta) = E(\theta) - E(0^\circ)$, illustrates that the vdW-DF-cx energy barrier ($\Delta E^{\text{vdW-DF-cx}}(50^\circ) \cong 18.56 \text{ meV/formula}$) is 9.16 meV/formula lower than that of PBEsol ($\Delta E^{\text{PBEsol}}(60^\circ) \cong 27.71 \text{ meV/formula}$) and the vdW-DF-cx rotational potential energy curve is broader than that of PBEsol.

Lowering of the vdW-DF-cx energy barrier attributes to the nature of electronic interaction incorporated in the xc-functionals and the distinction of optimised structures. To understand these, we calculate $\Delta E(\theta)$ of the vdW-DF-cx-structures for $\theta = 0^\circ$ to 60° , due to a symmetry of the energy curves, with applications of the following xc-functionals: vdW-DF-cx, PBEsol, vdW-DF-cx-ex (non-local correlation is turned off), and PBEsol-ex (PBEsol density gradient correlation is turned off) (see Fig. 2). The electronic interaction contribution can be observed by comparing $\Delta E^{\text{PBEsol(vdW-Str)}}$ with $\Delta E^{\text{vdW-DF-cx}}$. At $\theta = 60^\circ$, $\Delta E^{\text{PBEsol(vdW-Str)}}$ is $\sim 7.0 \text{ meV}$ higher than $\Delta E^{\text{vdW-DF-cx}}$ which reflects the fact that electronic non-local interaction lowers the rotational potential energy $\Delta E^{\text{PBEsol-ex(vdW-Str)}}$. Furthermore, since vdW-DF energy is split into semi-local (E_{xc}^0) and truly non-local (E_{xc}^{nl}) constituents, i.e. $E^{\text{vdw}} = E_{xc}^0 + E_{xc}^{nl}$, and the semi-local part of the vdW-DF-cx is chosen such that its

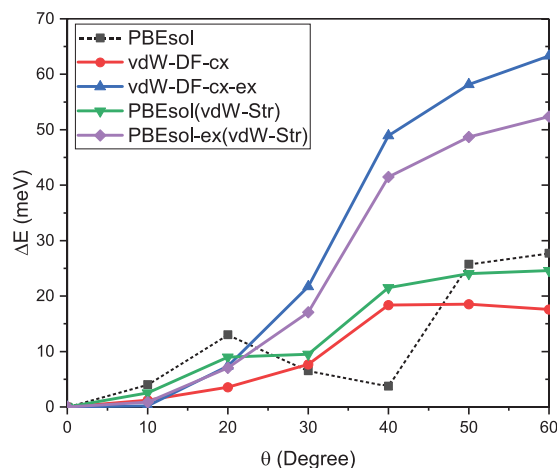


Figure 2. Rotational potential energy curves of the vdW-DF-cx-optimised structure calculated with vdW-DF-cx (red), PBEsol (green), PBEsol with gradient correction correlation off (purple), and vdW-DF-cx with nonlocal correlation off (blue). Dashed line is the rotational potential energy curve of the PBEsol-optimised structure.

exchange component resemble that of GGA-type xc-functional in the small-to-medium scaled density gradient regime³². One can read a difference between semi-local correlation and non-local correlation effects by comparing $\Delta E^{\text{PBEsol(vdW-Str)}} - \Delta E^{\text{PBEsol-ex(vdW-Str)}}$ with $\Delta E^{\text{vdW-DF-cx}} - \Delta E^{\text{vdW-DF-cx-ex}}$. PBEsol correlation is positive at $\theta = 10^\circ, 20^\circ$ while vdW-DF-cx correlation is negative at all rotational angles. Moreover, at these beginning rotational angles, the exchange parts of both semi-local and non-local xc-functionals are almost the same. The non-local correlation becomes crucially important at the moderate rotational angles ($\theta = 40^\circ, 50^\circ, 60^\circ$). The structural contribution can be perceived by comparing ΔE^{PBEsol} with $\Delta E^{\text{PBEsol(vdW-Str)}}$. This contribution attributes to: *i.* unit cell deformation (Fig. 3(a,b)), *ii.* I-displacement (octahedron distortion) (Fig. 3(c-e)), *iii.* MA arrangement and its internal distortion, and *iv.* hydrogen bonding (Fig. 4(b)). For instance, at $\theta = 60^\circ$, $\Delta E^{\text{PBEsol}} - \Delta E^{\text{PBEsol(vdW-Str)}} \cong 3.1$ meV (Fig. 2) is a consequence of: *i.* short PBE-optimised lattice vectors comparing to those of vdW-DF-cx-optimised structure while a difference in unit cell shearing is negligible, *ii.* notably large PBE-optimised I_2 atomic displacement in opposite of [100] direction comparing to that of vdW-DF-cx-optimised structures. Moreover, at this angle, only $\text{Hn}_1 - I_1^{(\text{bc})}$, $\text{Hn}_2 - I_1^{(\text{c})}$, and $\text{Hn}_3 - I_2^{(\text{a})}$ hydrogen bonds play the role (Fig. 4(b)), and those of PBEsol-optimised and vdW-DF-cx-optimised structures are almost the same. It is important to note here that the internal distortion of MA is negligible. Thus, $\Delta E^{\text{PBEsol}} > \Delta E^{\text{PBEsol(vdW-Str)}}$ mainly attributes to unit cell and octahedron deformations. The lowering of rotational potential barrier is predominated by the non-local interaction keeping H-atoms and I-atoms further apart from each other.

The broadening of vdW-DF-cx rotational potential energy curve can be related to an abrupt change of H-atom positions, illustrated in Fig. 4(a), accompanying with I_1 and I_3 displacements in [001] and [100] directions, respectively. These differences in optimised structures reflect the noticeable distinction in force field calculated by semi-local and non-local xc-functionals. This is emphasised by the totally difference in changes of C-N axis altitudinal angle when the MA undergo on-axis rotation shown in Fig. 3(f). This indicates the need for theoretical revision of dynamical properties of this material in which the truly non-local interaction is included as its importance has recently been realised in spin-polarised system³⁵ and nonmagnetic transition metals³⁶.

Furthermore, we examine the rotational potential energy when there are constraints imposed in structural relaxation process. The results are shown in Fig. 1(c). The vdW-DF-cx and PBEsol rotational energy barriers are 37.7 meV and 50.7 meV, respectively when the cell parameters are kept at the lowest energy configuration (B), and 50.6 meV and 47.0 meV, respectively, when both cell parameters and I-atomic positions are kept at the lowest energy configuration (C). We also calculate the free on-axis rotational frequencies corresponding to such energy barriers. By obeying the transition-state theory³⁰, the frequency is given by:

$$\nu = \frac{k_B T}{h} e^{-\Delta E/k_B T}$$

when ΔE is the rotational energy barrier. The obtained frequencies, at $T = 330$ K, for the relaxation model A, B, and C are 3.71 (2.60) THz, 1.83 (1.16) THz, and 1.16 (1.32) THz, respectively, for vdW-DF-cx (PBEsol) calculations. These rotational frequencies may help one experimentally justifies which MA rotational mechanism it is, if the local rotational frequency could be experimentally probed.

As we have seen in Fig. 4(b), even in this high symmetry phase the complexity of hydrogen bonding takes place in this material. Especially when MA undergoes rotation, the hydrogen bonding associated with a specific H-atom can be turned on/off or switches to bond with the other I-atom depending on the rotational angle. For example, Hn , strongly bonds with $I_3^{(\text{ab})}$ at $\theta \in [0^\circ, 40^\circ]$ then switches to strongly bond with $I_1^{(\text{bc})}$, (a criterion used for strong H-bond is $\text{H} \cdots \text{I} \leq 3 \text{ \AA}$). To illustrate that, we perform the maximally localised Wannier function

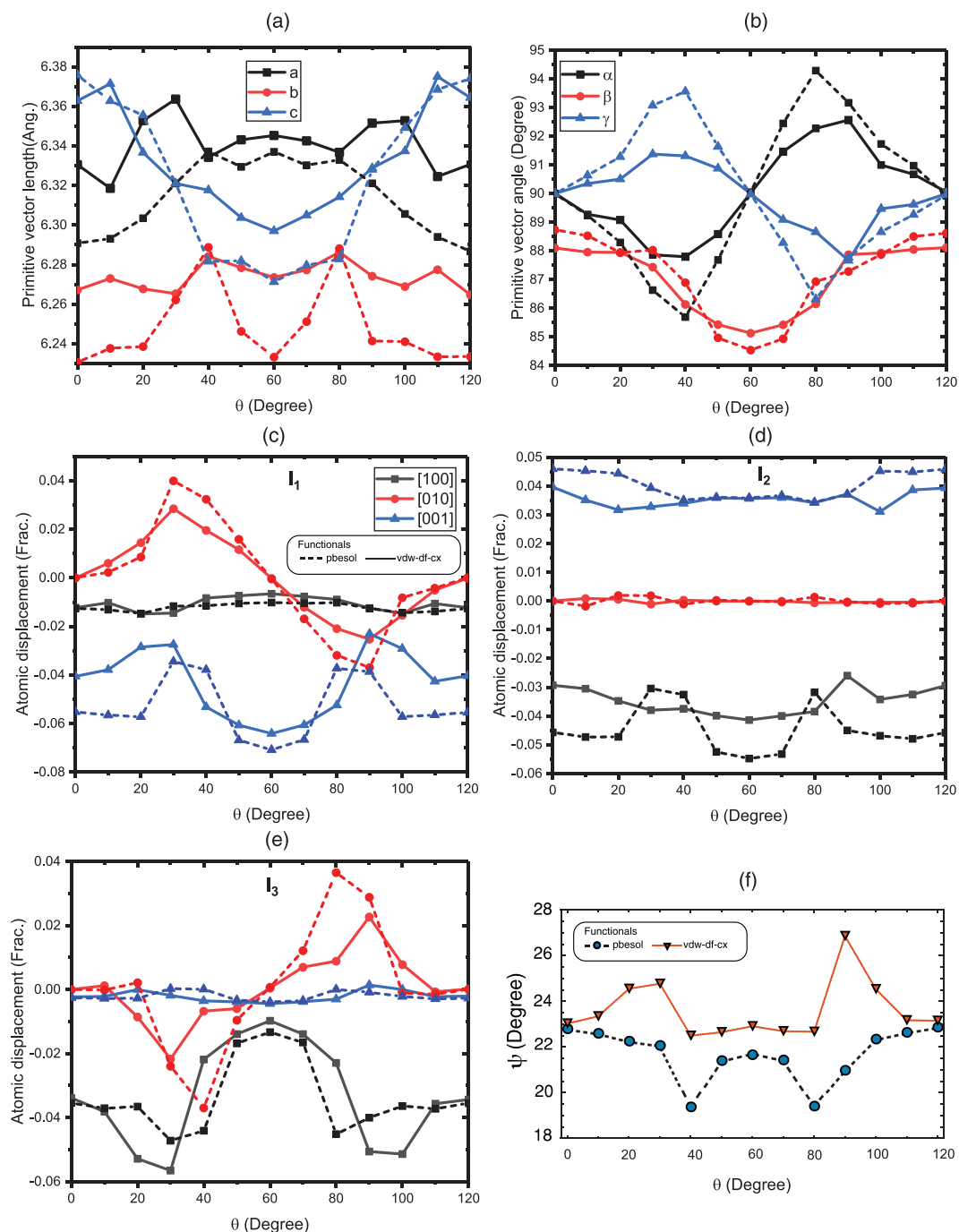


Figure 3. (a) Magnitudes of primitive vectors, (b) angles between them, and (c–e) atomic displacements (from Pb–I bond center) in crystallographic directions of three inequivalent I-atoms calculated by applying vdW-DF-cx (solid) and PBEsol (dashed) xc-functionals. (f) Altitudinal angle of C–N axis.

(MLWF) analysis by projecting the 25 bands Bloch manifold onto 12 atom-centred MLWFs manifold³⁷. The complete MLWFs calculated at $\theta = 0^\circ, 40^\circ, 60^\circ$ are given in supplementary information. Here, it is worth highlighting a MLWF that localised in vicinity of the $I_1^{(bc)}$ obtained at $\theta = 60^\circ$. This MLWF mainly has I-p lone pair atomic orbital character and, also, shows covalent bonding character with the $I_3^{(ab)}$ assisted by Hn_1 , see Fig. 5. Note that bond character identification of the hydrogen bond supported $I^- - I^-$ interaction is based on the basic idea of the quantum theory of atoms in molecules formulated by RFW. Bader³⁸ that the I-p lone pair of the $I_1^{(bc)}$ becomes delocalized into vicinity of the $I_3^{(ab)}$ instead of as localized as those of the other I-atoms. This result is the first direct theoretical evidence supporting the recently experimental observation of interstitial iodide migration that leads to I_2 formation in tetragonal $MAPbI_3$ via $2I^- \rightarrow I_2 + 2e^-$ and then material degradation with I_2 as a product^{39,40}. Moreover, recent experiment has revealed that I_2 can further accelerate the degradation of the iodide perovskites⁴¹. Notably, our results show that I–I covalent bonding is supported by hydrogen bond formed when

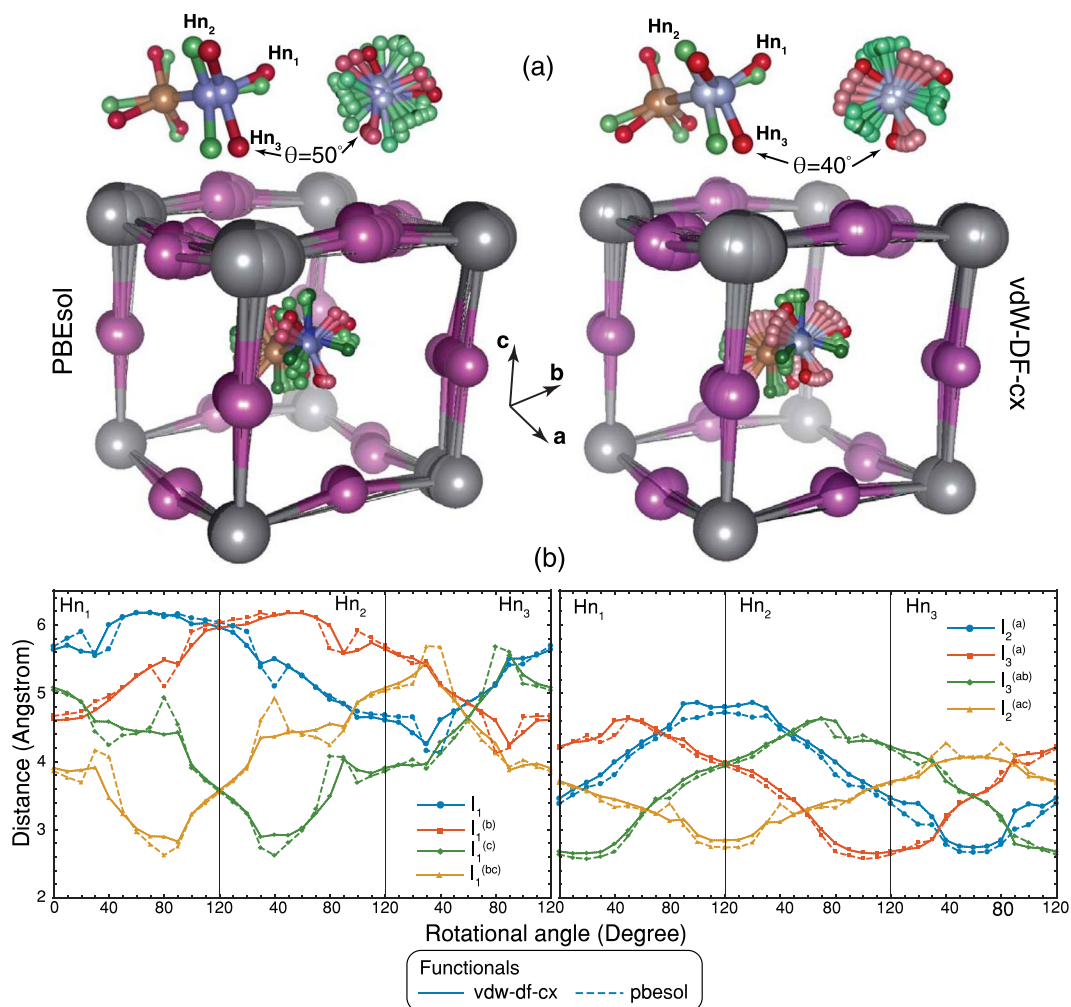


Figure 4. (a) Atomistic representations of optimised structures with PBEsol (left), and vdW-DF-cx (right) xc-functionals for $\theta = 10^\circ$ to 80° illustrate the abrupt changes in H-atom positions at $\theta = 50^\circ$ and $\theta = 40^\circ$ obtained by applying PBEsol and vdW-DF-cx xc-functionals, respectively. (b) H-I distances obtained by structural relaxation with application of vdW-DF-cx (solid) and PBEsol (dashed) xc-functionals where $I_i^{(xyz)}$ represent a replication of the I_i - atom obtained by performing translational symmetry operation with x, y, and z primitive vectors.

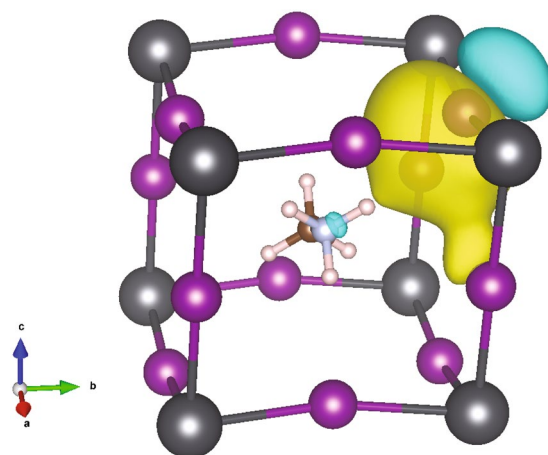


Figure 5. An isosurface of MLWF with the isosurface value = $\frac{\pm 1}{\sqrt{V}}$ calculated with vdW-DF-cx xc-functional at $\theta = 60^\circ$ where V is a unit cell volume in \AA^3 . Yellow and turquoise represent positive and negative values, respectively.

the structure is at the top of rotational potential hill which mean that I_2 formation is induced by MA rotation activated by thermal energy.

Conclusions

We have performed density functional theory (DFT) based calculations to investigate the equilibrium atomic configurations of the pseudocubic MAPbI_3 hybrid perovskite with respect to on-axis coherent methylammonium rotation. First, we assess the accuracy of a number of semi-local and non-local van der Waals exchange correlation density functionals (xc-functional) by calculating the structural parameters and compare them to the experimental values. According to the results in Table 1, vdW-DF-cx xc-functional shows the best overall performance for structural property DFT calculation of this material. Second, we report details of structural and energetic responses to the MA rotation obtained through the full structural relaxations. Comparison of results calculated with application of vdW-DF-cx with those of PBEsol xc-functionals shows noticeable lowering and broadening of vdW-DF-cx rotational potential energy curve. The non-local vdW correlation becomes crucial at the rotational angles (at $\theta = 40^\circ, 50^\circ, 60^\circ$) where the potential energy is much higher than the lowest energy (at $\theta = 0^\circ$). That manifest an inevitability of including truly non-local xc-functional in DFT study of this system. Also, the rotational potential barriers and corresponding rotational frequencies are calculated for the cases that the unit cell is fixed, and both unit cell and I-atom positions are fixed in the relaxation processes. Finally, a maximally localised Wannier function analysis reflects that the I – I covalent bonding can be formed at $\theta = 60^\circ$ with the assistance of hydrogen bonding. This can lead to I_2 formation and material degradation.

Methods

Static DFT calculation is performed with the pseudopotential and plane wave method implemented in Quantum-Espresso package⁴². The ion cores are represented by original scalar relativistic ultrasoft pseudopotentials taken from PSLibrary project⁴³. Spin-orbit coupling (SOC) effects are not included in this work, as previous study suggested that SOC does not significantly affect ground state properties of this material⁴⁴. The kinetic energy cut-off is set to 70 Ry. The unshifted k-point mesh is gridded into $6 \times 6 \times 6$ by Monkhorst-Packs scheme⁴⁵. This configuration yields convergence of total energy within 2 meV. The nonlocal vdW exchange correlation functionals considered in this work are as follows: rvv10⁴⁶, vdW-DF^{47,48}, vdW-DF2⁴⁹, vdW-DF-ob86⁵⁰ and vdW-DF-cx⁵¹. The Perdew-Burke-Ernzerhof (PBE)⁵² and PBEsol⁵³ functionals are also applied for comparison. The relaxation algorithm of atoms and lattice parameters used is Broyden-Fletcher-Goldfarb-Shanno (BFGS) algorithm with a force/atom tolerance equal to 0.001 Hartree/Bohr. The initial structure is the lowest enthalpy configuration reported by Brivio *et al.* study¹⁴ (available online⁵⁴) re-optimised with our settings. The calculations of exchange energies are achieved by setting of the Quantum-Espresso input variable, i.e. input_dft, as following: input_dft = 'sla + pw + cx13'; and input_dft = 'sla + pw + psx + nogc' for vdW-DF-cx and PBEsol exchange (with local correlation) density functionals respectively. For maximally localised Wannier function (MLWF) calculation, the k-space is meshed by $8 \times 8 \times 8$ grid. Twenty-five Bloch wave functions are projected onto twelve atom-centred MLWFs with convergent criteria of the spread function equal to 10^{-10} \AA^2 .

References

- Green, M. A., Ho-Baillie, A. & Snaith, H. J. The emergence of perovskite solar cells. *Nat. Photonics*. **8**, 506–514 (2014).
- Brenner, T. M., Egger, D. A., Kronik, L., Hodes, G. & Cahen, D. Hybrid organic-inorganic perovskites: low-cost semiconductors with intriguing charge-transport properties. *Nat. Rev. Mater.* **1**, 15007 (2016).
- Zheng, F., Saldana-Greco, D., Lui, S. & Rappe, A. M. Material innovation in advancing organometal halide perovskite functionality. *J. Phys. Chem. Lett.* **6**, 4862–4872 (2015). And references therein.
- Even, J. *et al.* Solid-state physics perspective on hybrid perovskite semiconductors. *J. Phys. Chem. C*. **119**, 1016–10177 (2015).
- Kojima, A., Teshima, K., Shirai, Y. & Miyasaka, T. Organometal halide perovskites as visible-light sensitizers for photovoltaic cells. *J. Am. Chem. Soc.* **131**, 6050–6051 (2009).
- Hodes, G. Perovskite-based solar cells. *Science* **342**, 317–318 (2013).
- National Renewable Energy Laboratory, C. Golden. Best research-cell efficiencies. http://www.nrel.gov/ncpv/images/efficiency_chart.jpg. Accessed July 19, 2016.
- Correa-Baena, J.-P. *et al.* The rapid evolution of highly efficient perovskite solar cells. *Energy Environ. Sci.* **10**, 710–727 (2017).
- Manser, J. S., Saidaminov, M. I., Christians, J. A., Bakr, O. M. & Kamat, P. V. Making and breaking of lead halide perovskites. *Acc. Chem. Res.* **49**, 330–338 (2016).
- Shahbazi, M. & Wang, H. Progress in research on the stability of organometal perovskite solar cells. *Solar Energy* **123**, 74–87 (2016).
- Pathak, S. *et al.* Atmospheric influence upon crystallization and electronic disorder and its impact on the photophysical properties of organic-inorganic perovskite solar cells. *ACS Nano* **9**, 2311–2320 (2015).
- Baikie, T. *et al.* Synthesis and crystal chemistry of the hybrid perovskite $(\text{CH}_3\text{NH}_3)\text{PbI}_3$ for solid-state sensitised solar cell applications. *J. Mater. Chem. A*. **1**, 5628–5641 (2013).
- Wang, Y. *et al.* Density functional theory analysis of structural and electronic properties of orthorhombic perovskite $\text{CH}_3\text{NH}_3\text{PbI}_3$. *Phys. Chem. Chem. Phys.* **16**, 1424–1429 (2014).
- Brivio, F. *et al.* Lattice dynamics and vibrational spectra of the orthorhombic, tetragonal, and cubic phases of methylammonium lead iodide. *Phys. Rev. B*. **92**, 144308–144316 (2015).
- Weller, M. T., Weber, O. J., Henry, P. F., Pumpo, A. M. D. & Hansen, T. C. Complete structure and cation orientation in the perovskite photovoltaic methylammonium lead iodide between 100 and 352 K. *Chem. Commun.* **51**, 4180–4183 (2015).
- Frost, J. M., Butler, K. T. & Walsh, A. Molecular ferroelectric contributions to anomalous hysteresis in hybrid perovskite solar cells. *APL Mater.* **2**, 081506 (2014).
- Frost, J. M. *et al.* Atomistic origins of high-performance in hybrid halide perovskite solar cells. *Nano Lett.* **14**, 2584–2590 (2014).
- Baikie, T. *et al.* A combined single crystal neutron/X-ray diffraction and solid-state nuclear magnetic resonance study of the hybrid perovskites $\text{CH}_3\text{NH}_3\text{PbX}$ ($X = \text{I, Br and Cl}$). *J. Mater. Chem. A*. **3**, 9298–9307 (2015).
- Mosconi, E., Quarti, C., Ivanovska, T., Ruani, G. & Angelis, F. D. Structural and electronic properties of organo-halide lead perovskites: a combined IR-spectroscopy and ab initio molecular dynamics investigation. *Phys. Chem. Chem. Phys.* **16**, 16137–16144 (2014).
- Quarti, C., Mosconi, E. & Angelis, F. D. Structural and electronic properties of organohalide hybrid perovskites from *ab initio* molecular dynamics. *Phys. Chem. Chem. Phys.* **17**, 9394–9409 (2015).

21. Ong, K. P., Goh, T. W., Xu, Q. & Huan, A. Structural evolution in methylammonium lead iodide $\text{CH}_3\text{NH}_3\text{PbI}_3$. *J. Phys. Chem. A* **119**, 11033–11038 (2015).
22. Deretzis, I. *et al.* Spontaneous bidirectional ordering of $\text{CH}_3\text{NH}_3\text{PbI}_3$ in lead iodide perovskites at room temperature: The origins of the tetragonal phase. *Sci. Rep.* **6**, 24443 (2016).
23. Leguy, A. M. A. *et al.* The dynamics of methylammonium ions in hybrid organic-inorganic perovskite solar cells. *Nat. Commun.* **6**, 7124 (2015).
24. Carignano, M. A. & Kachmar, A. Thermal effects on $\text{CH}_3\text{NH}_3\text{PbI}_3$ perovskite from *ab initio* molecular dynamics simulation. *J. Phys. Chem. C* **119**, 8991–8997 (2015).
25. Chen, T. *et al.* Rotational dynamics of organic cations in the $\text{CH}_3\text{NH}_3\text{PbI}_3$ perovskite. *Phys. Chem. Chem. Phys.* **17**, 31278–31286 (2015).
26. Li, B. *et al.* Polar rotor scattering as atomic-level origin of low mobility and thermal conductivity of perovskite $\text{CH}_3\text{NH}_3\text{PbI}_3$. *Nat. Commun.* **8**, 16086 (2017).
27. Li, J. & Rinke, P. Rotational dynamics of organic cations in the $\text{CH}_3\text{NH}_3\text{PbI}_3$ perovskite. *Phys. Rev. B* **94**, 045201–045212 (2016).
28. Motta, C., El-Mellouhi, F. & Sanvito, S. Exploring the cation dynamics in lead bromide hybrid perovskites. *Phys. Rev. B* **93**, 235412 (2016).
29. Lee, J. H., Bristowe, N. C., Bristowe, P. D. & Cheetham, A. K. Role of hydrogen-bonding and its interplay with octahedral tilting in $\text{CH}_3\text{NH}_3\text{PbI}_3$. *Chem. Commun.* **51**, 6434–6437 (2015).
30. Lee, J. H., Lee, J.-H., Kong, E.-H. & Jang, H. M. The nature of hydrogen-bonding in the prototypic hybrid halide perovskite, tetragonal $\text{CH}_3\text{NH}_3\text{PbI}_3$. *Sci. Rep.* **6**, 21687 (2016).
31. Hata, T., Giorgi, G. & Yamashita, K. The effects of organic-inorganic interactions on thermal transport properties of $\text{CH}_3\text{NH}_3\text{PbI}_3$. *Nano Lett.* **16**, 2749–2753 (2016).
32. Berland, K. & Hylgaard, P. Exchange functional that tests the robustness of plasmon description of the van der Waals density functional. *Phys. Rev. B* **89**, 035412 (2014).
33. Klimes, J., Bowler, D. R. & Michaelides, A. van der Waals density functional applied to solids. *Phys. Rev. B* **83**, 195131 (2011).
34. Ramalho, J. P. P., Gomes, J. R. B. & Illas, F. Accounting for van der Waals interactions between adsorbates and surfaces in density functional theory based calculations; selected examples. *RSC Adv.* **3**, 13085–13100 (2013).
35. Thonhauser, T. *et al.* Spin signature of nonlocal-correlation binding in metal organic frameworks. *Phys. Rev. Lett.* **115**, 136402 (2015).
36. Gharaee, L., Erhart, P. & Hyldgaard, P. Finite-temperature properties of nonmagnetic transition metals: Comparison of the performance of constraint-based semilocal and nonlocal functionals. *Phys. Rev. B* **95**, 085147.
37. Marzari, N., Mostofi, A. A., Yates, J. R., Souza, I. & Vanderbilt, D. Maximally localized Wannier functions: Theory and applications. *Rev. Mod. Phys.* **84**, 1419 (2012).
38. Bader, R. F. W. Definition of Molecular Structure: By Choice or by Appeal to Observation? *J. Phys. Chem. A*, 7431–7444 (2010)
39. Minns, J. L., Zajdel, P., Chernyshov, D., Beek, W. Van & Green, M. A. Structure and interstitial iodide migration in hybrid perovskite methylammonium lead iodide. *Nat. Commun.* **8**, 15152 (2017).
40. Ke, J. *et al.* *In situ* investigation of degradation at organometal halide perovskite surfaces by X-ray photoelectron spectroscopy at realistic water vapour pressure. *Chem. Commun.* **53**, 5231–5234 (2017).
41. Wang, S., Jiang, Y., Juarez-Perez, E. J., Ono, L. K. & Qi, Y. Accelerated degradation of methylammonium lead iodide perovskites induced by exposure to iodine vapour. *Nat. Energy* **2**, 16195 (2016).
42. Giannozzi, P. *et al.* Quantum espresso: a modular and open-source software project for quantum simulations of materials. *J. Phys. Condens. Matter* **21**, 395502 (2009).
43. Corso, A. D. Pslibrary. <http://www.qe-forge.org/gf/project/pslibrary/>. Accessed on 7th April 2018.
44. Umari, P., Mosconi, E. & De Angelis, F. Relativistic gw calculations on $\text{CH}_3\text{NH}_3\text{PbI}_3$ and $\text{CH}_3\text{NH}_3\text{SnI}_3$ perovskites for solar cell applications. *Sci. Rep.* **4**, 4467 (2014).
45. Monkhorst, H. J. & Pack, J. D. Special points for Brillouin-zone integrations. *Phys. Rev. B* **13**, 5188–5192 (1976).
46. Sabatini, R., Gorni, T. & de Gironcoli, S. Nonlocal van der Waals density functional made simple and efficient. *Phys. Rev. B* **87**, 041108 (2013).
47. Dion, M., Rydberg, H., Schroder, E., Langreth, D. C. & Lundqvist, B. I. Van der Waals density functional for general geometries. *Phys. Rev. Lett.* **92**, 246401 (2004).
48. Thonhauser, T. *et al.* Spin signature of nonlocal correlation binding in metal-organic frameworks. *Phys. Rev. Lett.* **115**, 136402 (2015).
49. Lee, K., Murray, E. D., Kong, L., Lundqvist, B. I. & Langreth, D. C. Higher-accuracy van der Waals density functional. *Phys. Rev. B* **82**, 081101 (2010).
50. Klimes, J. C. V., Bowler, D. R. & Michaelides, A. Van der Waals density functionals applied to solids. *Phys. Rev. B* **83**, 195131 (2011).
51. Berland, K. & Hylgaard, P. Exchange functional that tests the robustness of the plasmon description of the van der Waals density functional. *Phys. Rev. B* **89**, 035412 (2014).
52. Perdew, J. P., Burke, K. & Ernzerhof, M. Generalized gradient approximation made simple. *Phys. Rev. Lett.* **77**, 3865–3868 (1996).
53. Perdew, J. P. *et al.* Restoring the density-gradient expansion for exchange in solids and surfaces. *Phys. Rev. Lett.* **100**, 136406 (2008).
54. Brivio, F. *et al.* DFT optimised crystal structures of inorganic and hybrid halide perovskites. <https://github.com/WMD-group/hybrid-perovskites>. Accessed on 7th April 2018.

Acknowledgements

This research is supported by Rachadapisek Sompote Fund for Postdoctoral Fellowship, Chulalongkorn University and T.B. acknowledge support from Thailand Research Fund contract number RSA5880058. The computing resources are supported by National e-Science Infrastructure Consortium (NECTEC) at Large Scale Simulation Research Laboratory (LSR), National Science and Technology Development Agency (NSTDA), Thailand. Computing facilities have been partially supported by Sci-Super IV research grant, Faculty of Science and Ratchadapiseksomphot Endowment Fund of Chulalongkorn University (CU-59-046-EN).

Author Contributions

T.B. designed the research; all authors performed research, analysed the results. T.B., R.K. and V.S. wrote the manuscript.

Additional Information

Supplementary information accompanies this paper at <https://doi.org/10.1038/s41598-018-31462-x>.

Competing Interests: The authors declare no competing interests.

Publisher's note: Springer Nature remains neutral with regard to jurisdictional claims in published maps and institutional affiliations.



Open Access This article is licensed under a Creative Commons Attribution 4.0 International License, which permits use, sharing, adaptation, distribution and reproduction in any medium or format, as long as you give appropriate credit to the original author(s) and the source, provide a link to the Creative Commons license, and indicate if changes were made. The images or other third party material in this article are included in the article's Creative Commons license, unless indicated otherwise in a credit line to the material. If material is not included in the article's Creative Commons license and your intended use is not permitted by statutory regulation or exceeds the permitted use, you will need to obtain permission directly from the copyright holder. To view a copy of this license, visit <http://creativecommons.org/licenses/by/4.0/>.

© The Author(s) 2018